Soft Matter

PAPER

View Article Online
View Journal | View Issue

Check for updates

Cite this: *Soft Matter*, 2019, 15, 321

Small asymmetric Brownian objects self-align in nanofluidic channels

Giulia Fiorucci,[a] Johan T. Padding[b] and Marjolein Dijkstra*[a]

Received 23rd November 2018,
Accepted 7th December 2018

DOI: 10.1039/c8sm02384k

rsc.li/soft-matter-journal

Although the self-alignment of asymmetric macro-sized objects of a few tens of microns in size have been studied extensively in experiments and theory, access to much smaller length scales is still hindered by technical challenges. We combine molecular dynamics and stochastic rotation dynamics techniques to investigate the self-orientation phenomenon at different length scales, ranging from the micron to the nano scale by progressively increasing the relative strength of diffusion over convection. To this end, we model an asymmetric dumbbell particle in Hele-Shaw flow and explore a wide range of Péclet numbers (Pe) and different particle shapes, as characterized by the size ratio of the two dumbbell spheres ($\tilde{R}$). By independently varying these two parameters we analyse the process of self-orientation and characterize the alignment of the dumbbell with the direction of the fluid flow. We identify three different regimes of strong, weak and no alignment and we map out a state diagram in Pe *versus* $\tilde{R}$ plane. Based on these results, we estimate dimensional length scales and flow rates for which these findings would be applicable in experiments. Finally, we find that the characteristic reorientation time of the dumbbell is a monotonically decreasing function of the dumbbell anisotropy.

Published on 17 December 2018. Downloaded by Universiteit Utrecht on 1/17/2020 3:31:00 PM.

1 Introduction

In recent years microfluidic devices have found increasingly wide application in several scientific areas.[1] They are widely employed in clinical and biological research for disease diagnosis[2,3] and for cytometric analysis.[4] For instance, microfluidic techniques may be used to efficiently sort and analyse mixtures of healthy and diseased cells based on their differing physical properties.[5,6] Other applications are found in chemical and pharmaceutical industries, which use suspended micron-sized soft particles in confined flows as models to design deformable drugs delivery carriers.[7–10] The development of microfluidic technologies has opened new paths to manipulate suspended particles by having fine control over their position and orientation. Engineering particle trajectories in a device is now possible in three different ways, by means of external fields,[11] by taking advantage of hydrodynamic interactions in laminar flows, or by exploiting inertial effects in flow drag at finite Reynolds numbers.[12] The latter has been achieved in recent studies on flow sculpting,[13–15] while hydrodynamic interactions are exploited in laminar flows by engineering the geometry of the channel[16–20] or, alternatively, the shape of the suspended particles.[21–23] This work is concerned with the last of these and specifically with dumbbell shaped particles. Such a particle, consisting of two connected disks, transported in a Hele-Shaw flow exhibits a rich variety of dynamic behaviours,[22] which are induced entirely by hydrodynamic interactions (HIs). By fine-tuning the relative size of the two disks, it is possible to control the trajectory of the particle. A comprehensive experimental and theoretical study is reported in ref. 22, where the authors investigated the non-Brownian regime. A recent work has further analysed this particular system, providing an alternative and more efficient theoretical framework to solve the Stokes flow around the particle.[23] Their study focuses on the already known phenomenon of self-orientation, the spontaneous alignment of the long axis of the particle with the flow direction, provided that the two disks have different radii ($R_1 \neq R_2$). This phenomenon originates from the hydrodynamic self-interaction, *i.e.* the hydrodynamic interactions the two disks exert on each other. In the present case of high confinement, a disk with diameter $2R_1$ generates a flow disturbance which decays with distance r as a dipole field $\propto 2R_1/r^2$. In addition, the magnitude of the generated velocity field linearly increases with the diameter of the disk. In case of a symmetric dumbbell, where the two disks have equal radii ($R_1/R_2 = \tilde{R} = 1$), the hydrodynamic force that disk 1 exerts on disk 2 is perfectly balanced by the force disk 2 exerts on disk 1, resulting in only a lateral drift of the particle without any rotation. However if the dumbbell is asymmetric ($R_1 > R_2$, $\tilde{R} > 1$) the imbalance of internal hydrodynamic forces results in a torque on the dumbbell that must be balanced by a frictional

[a] *Soft Condensed Matter, Debye Institute for Nanomaterials Science, Department of Physics, Utrecht University, Princetonplein 1, 3584 CC, Utrecht, The Netherlands. E-mail: m.dijkstra@uu.nl; Tel: +31 30 253 3270*

[b] *Process and Energy Department, TU Delft, Leeghwaterstraat 39, 2628 CB, Delft, The Netherlands*

Published on 17 December 2018. Downloaded by Universiteit Utrecht on 1/17/2020 3:31:00 PM.

torque of rigid rotation, which causes the small disk to be dragged downstream of the large disk.

Although this specific system has been extensively examined, the studies performed so far concern macro-sized particles, which are much less affected by thermal fluctuations as compared to colloids, polymer chains or macromolecules. The experiments[22] were performed at very high Pe number (on the order of 10^4), which was essential to drag particles of a few tens of microns in width and 100 microns in length, dimensions that are quite big if compared to the typical colloidal length scales (100–1000 nm). Similarly, in numerical studies,[22–24] the lack of thermal noise in the deterministic model limits the investigations to infinite Pe and do not provide insights on the possibility of self-orientation of smaller objects.

On the basis of these arguments, natural questions arise: is the self-alignment still possible for nanoparticles or macromolecules with an asymmetric conformation? What is the effect of thermal fluctuations on the self-orienting process? The progressively increasing interest in nanofluidics for "lab-on-a-chip" bioanalysis techniques and for DNA manipulation,[25] leads to an urgent need to bridge these length scales and to verify whether self-organization can still be exploited down to the nanoscale. In this study, we show for the first time, at the best of our knowledge, that very small Brownian objects can exhibit self-alignment in nanofluidic channels. To do so, we combine molecular dynamics and stochastic rotation dynamics techniques (MD + SRD) to simulate a dumbbell particle in a Hele-Shaw flow. This hybrid technique naturally includes hydrodynamic interactions as well as thermal fluctuations, and will be described in more detail in Section 2.2. In addition it enables us to arbitrarily tune the relative strength of the convection over the diffusion. This study aims to explore the Brownian regime where both thermal fluctuations and hydrodynamic interactions are important. In particular, we analyse the self-orientation phenomenon and the stability of the alignment with the flow by exploring a wide range of Péclet numbers, from the fully-Brownian regime towards the non-Brownian regime, and different particle shapes.

2 Model and methods

2.1 The dumbbell in geometrical confinement

We perform numerical simulations (MD + SRD) to study the effect of Brownian fluctuations on the self-orientation process of a single dumbbell particle transported by a pressure-driven flow. In Fig. 1(a) we present a schematics of the system. We consider a shallow channel with a rectangular cross section. The confining walls are orthogonal to the x and y axes, while we implement periodic boundary conditions (PBC) along the z axis. The height of the channel is H and the width is W. The fluid flows with an approximately uniform maximal velocity U_0 parallel to the z axis, as shown by the black arrows in the figure, and it drags the dumbbell particle embedded in the fluid. The dumbbell is composed of two colloidal spheres with radii R_1 and $R_2 \leq R_1$. Note that we use spheres instead of disks as in ref. 22 and 23, because dumbbell spheres are simpler to simulate and

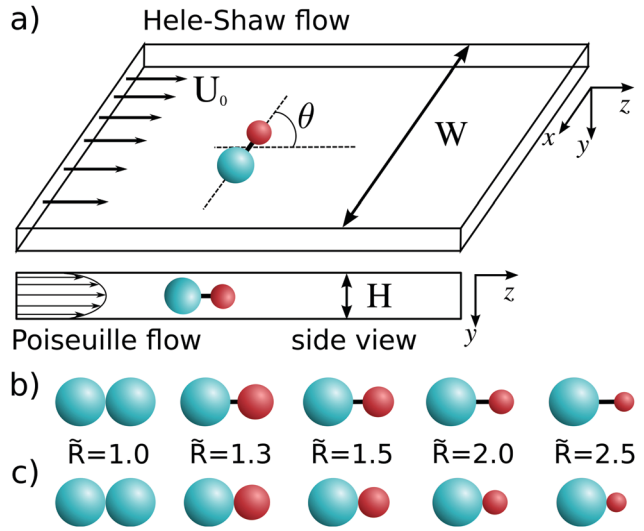

Fig. 1 Schematics of the system. Dumbbell particle flowing at the centre of a 3D channel of a rectangular cross section transported by the fluid flow at constant pressure gradient (a). Model of a dumbbell particle composed of two spheres of radius R_1 and $R_2 \leq R_1$. We model five different dumbbell shapes by varying the sphere size ratio $\tilde{R} = R_1/R_2$. The center-to-center equilibrium distance $s = 8.8\ a_0$ is kept constant (b), or changes with $\tilde{R}$ as $s = R_1 + R_2$ (c). Note that the particle longitudinal axis can slightly wiggle in the yz plane, therefore we define the angle $\theta \in (-180°, 180°]$ as the angle between the projection of the particle axis on the xz plane and the z axis.

easier to create experimentally at the small (colloidal) scales where Brownian motion is relevant. The spheres are bounded by a harmonic potential $\beta U_h(r_{12}) = k(r_{12} - s)^2/2\ a_0^2$, where $\beta = 1/k_B T$ is the inverse temperature, k_B is the Boltzmann constant and T is the temperature. The instantaneous center-to-center distance of the spheres is $r_{12} = |\mathbf{r}_2 - \mathbf{r}_1|$, with the spheres at positions $\mathbf{r}_1$ and $\mathbf{r}_2$, respectively. The parameter s denotes the equilibrium distance and a_0 our unit of length, to be defined later. The parameter k is a dimensionless harmonic spring constant. We choose $k = 10^5$ such that the characteristic period of elastic vibration of the dumbbell is much smaller than the time needed for the acoustic wave in the fluid to travel over the particle radius. The phenomenon of self-orientation depends sensitively on the shape of the particle, as characterized by the size ratio $\tilde{R} = R_1/R_2$. To investigate the effect of particle shape on the hydrodynamic self-orientation, we consider dumbbells with five different size ratios. The radius of the cyan sphere R_1 is kept constant, whereas the radius of the red sphere R_2 is varied. We test two models, in the first s is held constant for different size ratios at a value of 8.8 a_0, while in the second $s = R_1 + R_2$, as illustrated in Fig. 1(b) and (c), respectively. The interaction between each sphere of the dumbbell and the confining walls is described by a purely repulsive Weeks–Chandler–Andersen (WCA) potential[26]

$$\beta\phi_{cw}(r_i) = \begin{cases} 4\beta\varepsilon_{cw}\left[\left(\frac{\sigma_{cw}}{r_i}\right)^{12} - \left(\frac{\sigma_{cw}}{r_i}\right)^{6} + \frac{1}{4}\right] & r_i \leq 2^{1/6}\sigma_{cw} \\ 0 & r_i > 2^{1/6}\sigma_{cw}, \end{cases} \quad (1)$$

 This journal is © The Royal Society of Chemistry 2019

Published on 17 December 2018. Downloaded by Universiteit Utrecht on 1/17/2020 3:31:00 PM.

where r_i is the distance along $i = \{x,y\}$ between the center of the sphere and the surface of the wall, $\varepsilon_{cw} = 40k_BT$ sets the colloid-wall energy scale and σ_{cw} represents the colloid–wall collision radius. The dimensions of the channel are $W \times H = 100 \times 10\ a_0^2$. The length of the channel along the z direction, L_z, is chosen to be sufficiently large that the hydrodynamic interactions of the dumbbell particle with its own periodic image can be neglected. In a quasi-2D system, the flow disturbance generated by the presence of the particle decays as $4R_1^2/r^2$, hence the disturbance is less than 0.1% for $r = 100\ R_1$, and with a typical R_1 of 4 a_0 we therefore choose $L_z = 400\ a_0$. We choose $\sigma_{cw} = 4.4\ a_0$ for the largest sphere, such that it is highly confined in the y direction, leaving a lubricating gap of 0.6 a_0 to the wall. Position $\mathbf{R}_i$ and velocity $\mathbf{V}_i$ of each sphere i are integrated *via* the velocity Verlet algorithm[27]

$$\mathbf{R}_i(t+\Delta t_{MD}) = \mathbf{R}_i(t) + \mathbf{V}_i(t)\Delta t_{MD} + \frac{\mathbf{F}_i(t)}{2M_i}\Delta t_{MD}^2, \quad (2)$$

$$\mathbf{V}_i(t+\Delta t_{MD}) = \mathbf{V}_i(t) + \frac{\mathbf{F}_i(t)+\mathbf{F}_i(t+\Delta t_{MD})}{2M_i}\Delta t_{MD}, \quad (3)$$

over a timestep Δt_{MD}. $\mathbf{F}_i(t)$ is the force acting on sphere i at time t and M_i is the mass of the sphere. We match the mass density of each dumbbell bead with the mass density of the fluid.

2.2 The fluid

The MD + SRD method was introduced by Malevanets and Kapral in 1999.[28,29] Since then it has been implemented to study a large variety of systems. For example, it has been employed to study the fluid flow in confinement, or driven by an external force.[30] In addition, it has been applied to investigate polymers in solution[31] or the sedimentation in colloidal suspensions.[32] Moreover this technique is particularly convenient for the study of colloidal suspensions embedded in a fluid, since the intrinsically stochastic nature of the algorithm naturally incorporates the thermal noise,[28] *i.e.* it automatically captures the Brownian fluctuations experienced by the colloidal particles in a suspension. Within MD + SRD the fluid is represented by the explicit presence of coarse-grained point particles of mass m_f, whose positions and velocities are continuous variables in space. Hence we refer to these point particles as "fluid particles", even if the physical properties of the fluid are not represented at the single particle level, but are rather extracted from a local average. Fluid particles are subjected to Newton's laws of motion and their positions and velocities are integrated *via* the MD scheme. This is the streaming step of the simulation method, where we implement the velocity Verlet algorithm[27]

$$\mathbf{r}_i(t+\Delta t_{MD}) = \mathbf{r}_i(t) + \mathbf{v}_i(t)\Delta t_{MD} + \frac{\mathbf{f}_i(t)}{2m_f}\Delta t_{MD}^2, \quad (4)$$

$$\mathbf{v}_i(t+\Delta t_{MD}) = \mathbf{v}_i(t) + \frac{\mathbf{f}_i(t)+\mathbf{f}_i(t+\Delta t_{MD})}{2m_f}\Delta t_{MD}, \quad (5)$$

where Δt_{MD} is the integration time step, $\mathbf{r}_i$ and $\mathbf{v}_i$ are, respectively, the position and the velocity of particle i, which is subject to the total force $\mathbf{f}_i$. In the streaming step fluid particles do not interact with each other and behave as an ideal gas. Therefore the total force acting on a fluid particle arises from the colloid–fluid interaction and the pressure gradient imposed externally. While executing the collision step, the SRD algorithm enables the exchange of momentum throughout the solvent performing coarse-grained collisions among the fluid particles. Every time interval $\Delta t_c = 4\Delta t_{MD}$ we partition the volume of the system into cubic cells (SRD cells of size a_0^3), we compute the center of mass velocity $\mathbf{v}_{cm}$ in each cell, and we rotate the relative velocities by a fixed angle $\alpha = \pi/2$ about a randomly oriented axis[33]

$$\mathbf{v}_i^{new} = \mathbf{v}_{cm} + \mathscr{R}(\alpha) \times (\mathbf{v}_i^{old} - \mathbf{v}_{cm}), \quad (6)$$

where $\mathbf{v}_i^{old}$ and $\mathbf{v}_i^{new}$ are the velocities of particle i before and after the collision step, respectively, and $\mathscr{R}$ is the rotation matrix. We shift the SRD cells before performing the collision step, in order to maintain Galilean invariance.[34,35] The SRD method locally conserves both energy and momentum, which is crucial for correctly reproducing the Navier–Stokes hydrodynamics.[28] In order to generate a fluid flow, as shown in Fig. 1, we apply an external driving force on the fluid particles. The force is parallel to the z direction. In order to maintain a constant temperature of the fluid, we implement a modified version of the stochastic thermostat proposed by Heyes,[36] which is extensively described in ref. 37. To ensure the velocity of the fluid is zero at the wall, we impose no-slip boundary condition by implementing the bounce-back rule.[28] We also insert virtual particles into the SRD cells that are overlapping with the wall when performing the collision step[30] in order to prevent spurious slip. The fluid is represented by $N_f = 2 \times 10^6$ particles, *i.e.* 5 particles per cell, corresponding to a mass density $\rho_f = 5\ m_f/a_0^3$. The fluid particles interact with the dumbbell through the repulsive WCA potential

$$\beta\phi_{cf}(r) = \begin{cases} 4\beta\varepsilon_{cf}\left[\left(\frac{\sigma_{cf}}{r}\right)^{12} - \left(\frac{\sigma_{cf}}{r}\right)^{6} + \frac{1}{4}\right] & r \le 2^{1/6}\sigma_{cf} \\ 0 & r > 2^{1/6}\sigma_{cf}, \end{cases} \quad (7)$$

where $\varepsilon_{cf} = 2.5k_BT$ sets the colloid–fluid energy scale and σ_{cf} is the colloid–fluid collision radius. We remark that σ_{cf} should be smaller than σ_{cw} to prevent the effect of spurious depletion that might arise between colloid and wall.[33] Therefore we impose $\sigma_{cw} = 1.1\ \sigma_{cf}$. In addition, we highlight that we implement the slip boundary condition on the surface of the colloidal particle; this property naturally comes from the isotropic property of the colloid–fluid interaction potential.

The different hydrodynamic regimes are characterised by dimensionless numbers that determine the relative importance of the different physical processes. The dependence of these dimensionless numbers on the simulation parameters are described in ref. 33. First, we ensure that the fluid modelled by SRD particles reproduces a liquid-like rather than a gas-like dynamics. The Schmidt number $Sc = \nu/D_f$, defined by the rate of diffusive momentum transfer over the rate of diffusive mass transfer in the fluid, distinguishes between these two different behaviours. When momentum transfer results from collisions

Published on 17 December 2018. Downloaded by Universiteit Utrecht on 1/17/2020 3:31:00 PM.

among particles rather than mass diffusion, the SRD fluid represents a liquid and Sc $\gg$ 1. In our simulations, the Schmidt number Sc $>$ 6 is sufficiently high to guarantee liquid-like dynamics. Second, we ensure that the Mach number[38] Ma = U_0/c_f, which compares the velocity of the fluid U_0 with respect to the speed of sound c_f, is small enough to avoid compressibility effects so that the fluid can be assumed to be effectively incompressible. Hence, we set Ma $\sim$ 0.1 in our simulations. Another important parameter is the Reynolds number[38] Re = $U_0\sigma_{cf}\rho_f/\eta$ which measures the relevance of inertial over viscous forces and where η denotes the shear viscosity of the fluid. We simulate a fluid in the Stokes regime, *i.e.* in absence of turbulence. The critical Reynolds number $\mathrm{Re_c}$, which discriminates the crossover from laminar to turbulent flow, depends on the physical system under investigation. It is known that $\mathrm{Re_c} \sim 1$ in bulk[33] while it has been recently shown that the critical thresholds is higher in a channel ($\mathrm{Re_c} \sim 800$)[39] and much higher in a pipe ($\mathrm{Re_c} \sim 2000$).[40] In our simulations Re $<$ 0.8, which corresponds to Stokes flow. In the present work we perform simulations exploring a wide range of Péclet numbers. This parameter measures the relevance of convective over diffusive transport, and we define it as follows

$$\mathrm{Pe} = \frac{U_0 R_1}{D_0}, \tag{8}$$

where R_1 and D_0 are, respectively, the radius and the bare diffusion coefficient of the larger sphere. We chose R_1 as a representative quantity for the size of the dumbbell as it remains constant upon varying the size ratio $\tilde{R}$, and hence Pe and $\tilde{R}$ can be changed independently. To explore different hydrodynamic regimes, we vary the shear viscosity of the fluid η. More specifically in terms of simulation parameters, we change the integration time step from $\Delta t_{\mathrm{MD}} = 0.025\ t_0$ for Pe $\sim$ 40, to $\Delta t_{\mathrm{MD}} = 1.75 \times 10^{-3}\ t_0$ for Pe $\sim$ 500, being $t_0 = a_0\sqrt{m_f/k_B T}$. With this choice of parameters the shear viscosity varies from $\eta = 2.5\,\eta_0$ to $\eta = 32\,\eta_0$, respectively, with $\eta_0 = m_f/(a_0 t_0)$.

2.3 Achieving steady state flow of the fluid

During the self-orientation process the asymmetric dumbbell changes its orientation and eventually aligns with the fluid flow with the small sphere dragged downstream of the large sphere. This phenomenon is determined by the hydrodynamic self-interaction, while the hydrodynamic interaction with the side walls (the walls orthogonal to the x axis) plays no role in this process.[22] We position the particle's center of mass at the center of the channel $x = 0$, with orientation $\theta = 170^\circ$, where $\theta \in (-180^\circ, 180^\circ]$ is defined as the angle between the projection of the particle's long-axis on the xz plane and the z axis (see Fig. 1(a)). Before proceeding with the measurements of the angle θ over time, we wait till the fluid forms the expected velocity profile. In order to achieve this steady state without affecting the initial orientation of the dumbbell, we initially impose a constraint on the dumbbell, such that the acceleration of the two spheres along the y and the z axes are the same, while the acceleration of the center of mass along the x axis is zero. This can be achieved by imposing the following forces on the large particle (here with label 1)

$$\begin{aligned} F_{x1}^{\mathrm{new}} &= F_{x1} - \frac{\mu}{M_2}(F_{x1} + F_{x2}) \\ F_{y1}^{\mathrm{new}} &= \frac{\mu}{M_2}(F_{y1} + F_{y2}) \\ F_{z1}^{\mathrm{new}} &= \frac{\mu}{M_2}(F_{z1} + F_{z2}), \end{aligned} \tag{9}$$

where $\mu = M_1 M_2/(M_1 + M_2)$ is the reduced mass, M_j is the mass of sphere j and F_{ij} is the instantaneous force along i experienced by sphere j. Similarly, the forces imposed on the small particle (labelled 2) can be obtained from (9) by exchanging the subscripts 1 and 2. Once the expected velocity profile is formed, we release the constraints and start our measurements. The velocity profile of the fluid along the z direction is determined by the specific geometry of the channel. In our case, we expect to observe a parabolic profile (Poiseuille flow) from the side view because of the high confinement in the y axis, while we expect an approximately uniform profile (Hele-Shaw flow) from the top view.

3 Results

3.1 Verification of fluid velocity profile

In Fig. 2 we report the fluid velocity profile u_z from the top view at different heights y of the channel, and from the side view at $x = 50\ a_0$. The points represent our numerical results, obtained by averaging the velocities of the fluid particles over the volume of a single SRD cell (a_0^3). The profiles are in very good agreement with the theoretical prediction,[41] represented here by the solid lines. We highlight that there is no adjustable parameter for the magnitude of the velocity field. However, our profile extrapolates to a finite non-zero velocity at the wall, and therefore

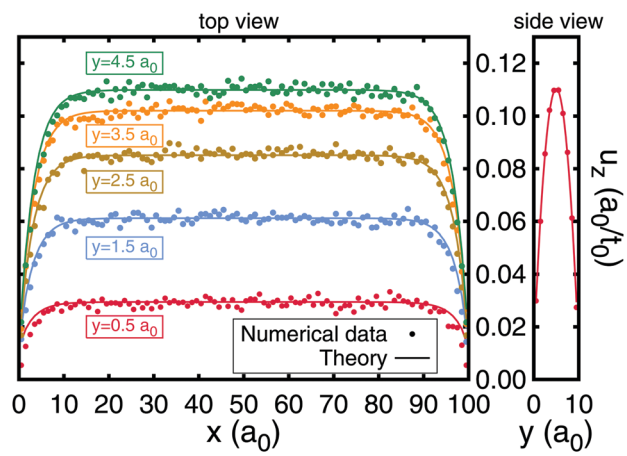

Fig. 2 Velocity profile of the fluid flow u_z along x and y at different heights. The dots represent the results obtained with the MD + SRD method, while solid lines are theoretical predictions. The profile is determined by the geometry of the channel. In this shallow channel we observe almost a flat profile (Hele-Shaw flow) from the top view, where different colors denote velocity profiles at different heights along the y axis, and a parabolic profile (Poiseuille flow) from the side view, where we show the profile at $x = 50.0\ a_0$.

 This journal is © The Royal Society of Chemistry 2019

Published on 17 December 2018. Downloaded by Universiteit Utrecht on 1/17/2020 3:31:00 PM.

we obtain the best fit by including a small slip velocity of magnitude $\sim 0.01\ a_0/t_0$.

3.2 Hydrodynamic self-orientation: the state diagram

We perform MD + SRD simulations on a single dumbbell particle with fixed $s = 8.8\ a_0$ as shown in Fig. 1(b) in a fluid flow. We study the self-orientation process by measuring the angle θ of the long-axis of the dumbbell with the flow direction as a function of time. Note that our model consists of a dumbbell in three dimensions which can slightly wiggle in the yz plane. Hence the angle θ is defined as the angle between the xz projection of the particle center-to-center axis and the z axis. For example, we plot the angle θ as a function of the reduced time $\tilde{t} = tU_0/s$ for Pe = 480 and $\tilde{R} = 1.3$ in Fig. 3(a). Each curve in the plot represents a single run performed at the same physical conditions. We simulated eight independent runs in order to investigate the statistical fluctuations. All the curves show essentially the same trend. The simulation is initiated with a dumbbell particle forming an angle $\theta = 170^\circ$ with the direction of the fluid flow. After a certain waiting time, the value of θ rapidly decreases towards $\theta = 0^\circ$, where it remains stable over time within small fluctuations due to the thermal noise. Note that at this apparently high Pe Brownian fluctuations are still visible, but, contrary to the case of the Brownian regime, they do not significantly interfere with the hydrodynamic drag and the resulting particle orientation. The thermal noise is not only the cause of the small fluctuations about the equilibrium orientation at $\theta = 0^\circ$ but it also prevents the immediate reorientation of the dumbbell: the configuration characterized by $\theta \simeq 180^\circ$ is an unstable equilibrium configuration,[22] therefore the hydrodynamic torque about this angle is still quite weak compared to the Brownian fluctuations. Consequently, the competition between the hydrodynamic torque, which leads to the reorientation of the particle, and the Brownian fluctuations, determines the different waiting times at which the particle starts reorienting. In Fig. 3(a) we clearly observe this phenomenon by comparing eight independent runs. Nevertheless the different waiting times do not affect the self-alignment process itself. Once the hydrodynamic forces start to dominate, the change in θ with time for intermediate angles is very similar in the eight runs. This is most clearly appreciated by the similarity of the slopes around $\theta = 90^\circ$, in fact the typical time scale of the self-orientation process is only intrinsically related to the shape of the particle, parametrized here by $\tilde{R}$, and the geometry of the channel. Later in this section we will provide quantitative results on this topic, while for the moment we focus on the alignment of the particle once the self-orientation has occurred. Specifically, we investigate how the alignment is destabilized by the thermal fluctuations as we decrease the Péclet number. In addition, we show that as we enter the Brownian regime, the stability of the alignment depends also on the shape of the particle, therefore we will also compare the behaviour at constant Pe and different $\tilde{R}$.

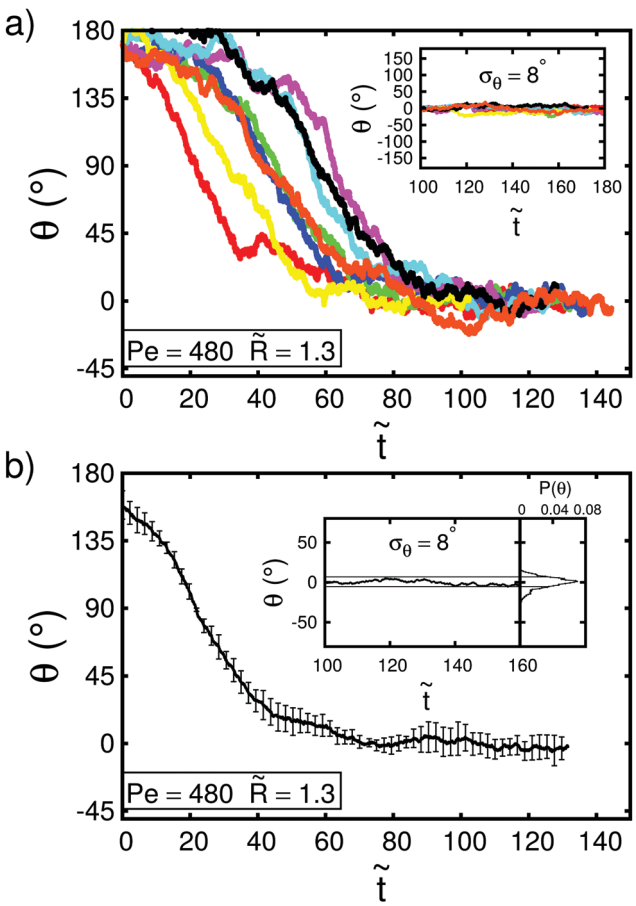

Fig. 3 (a) The tilt angle θ of the long-axis of the dumbbell with the flow direction as a function of reduced time $\tilde{t} = tU_0/s$ for a dumbbell with $s = 8.8\ a_0$ and size ratio $\tilde{R} = 1.3$ in a channel under an external flow at Pe = 480. Different curves represent independent runs. The graph shows the self-orientation process where the particle is initially positioned with $\theta = 170^\circ$ and, due to the hydrodynamic self-interaction, it eventually aligns with the fluid flow ($\theta = 0^\circ$). The inset shows fluctuations of θ about the equilibrium value $\theta = 0^\circ$ as a function of $\tilde{t}$ for simulation runs where the dumbbell is initially positioned with $\theta = 0^\circ$. We measure the standard deviation of θ obtaining $\sigma_\theta = 8^\circ$. (b) Tilt angle θ averaged over eight runs presented in (a). Inset: The left panel shows the tilt angle θ averaged over eight runs in (a), the right panel shows the normalised histogram of θ. The horizontal lines indicate the full width at half maximum.

As we lower the Péclet number we enhance the strength of the thermal noise relative to the strength of the convective flux. We compare Fig. 3(b), 4(a) and (b) where we show the tilt angle θ averaged over eight realizations as a function of time, for $\tilde{R} = 1.3$ and Pe = 480, Pe = 170 and Pe = 40, respectively. It is apparent that the curves present larger errorbars as we lower the Péclet number, moreover the fluctuations in orientation about the equilibrium position $\theta = 0^\circ$ are more pronounced. To quantify the magnitude of these oscillations we measure the standard deviation of the angle θ with respect to its mean value $\langle\theta\rangle$ as $\sigma_\theta = \sqrt{\langle\theta^2\rangle - \langle\theta\rangle^2}$. By decreasing Pe, we observe an increase of σ_θ, as shown in the inset of Fig. 3(b) and 4. Here we also display the histogram of θ, which broadens up as Pe decreases. This is clear evidence that decreasing the Péclet number destabilizes the alignment of the particle at $\theta = 0^\circ$, which is the hydrodynamically stable configuration.

The Péclet number is a good parameter to estimate the relevance of the thermal fluctuations compared to the hydrodynamic drag, but it is not sufficient to give a complete description

Published on 17 December 2018. Downloaded by Universiteit Utrecht on 1/17/2020 3:31:00 PM.

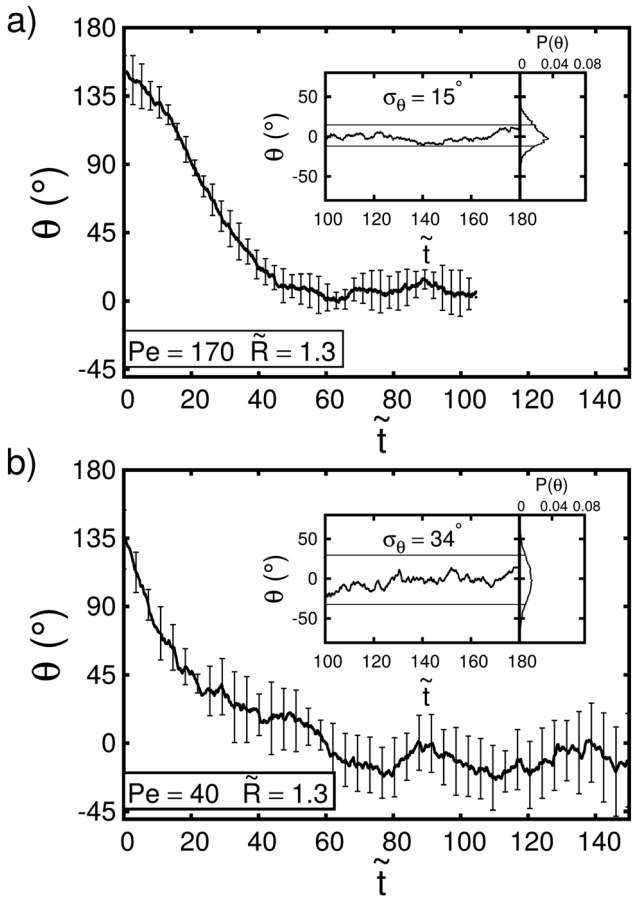

Fig. 4 Tilt angle θ averaged over eight realizations as a function of reduced time $\tilde{t} = tU_0/s$ for a dumbbell with $s = 8.8\ a_0$ and size ratio $\tilde{R} = 1.3$ in a channel under an external flow at Pe = 170 (a) and Pe = 40 (b). By decreasing Pe the curves presents larger fluctuations and σ_θ increases, being $\sigma_\theta = 15^\circ$ in (a) and $\sigma_\theta = 34^\circ$ in (b). Inset: The left panel shows the tilt angle θ averaged over eight runs, the right panel shows the normalised histogram of θ. The horizontal lines indicate the full width at half maximum.

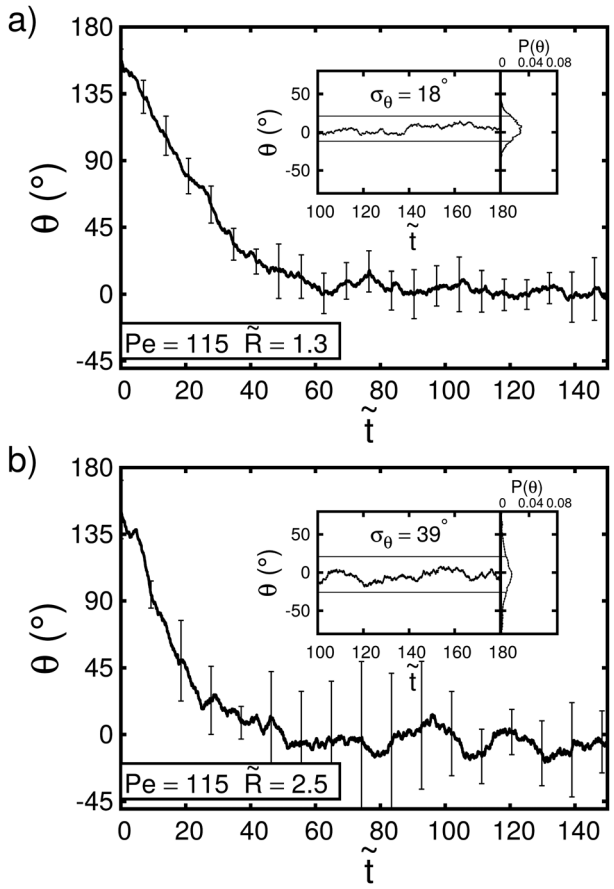

Fig. 5 Tilt angle θ averaged over eight realizations as a function of reduced time $\tilde{t} = tU_0/s$ for a dumbbell with $s = 8.8\ a_0$ and size ratio $\tilde{R} = 1.3$ (a) and $\tilde{R} = 2.5$ (b) in a channel under an external flow at Pe = 115. By increasing $\tilde{R}$ the curves exhibits larger fluctuations and σ_θ increases, being $\sigma_\theta = 18^\circ$ in (a) and $\sigma_\theta = 39^\circ$ in (b). Inset: The left panel shows the tilt angle θ averaged over eight runs, the right panel shows the normalised histogram of θ. The horizontal lines indicate the full width at half maximum.

of the stability of the particle. From the definition given in eqn (8) it is clear that Pe does not depend on the specific shape of the particle, only on its typical length scale. However we expect that the stability is also related to the shape of the dumbbell. For instance we intuitively expect that as we decrease the radius of sphere 2, the thermal fluctuations become more effective, leading to destabilization. We therefore investigate also the behaviour of the dumbbell by allowing $\tilde{R}$ to vary while we keep Pe constant. In analogy to the previous analysis, we compare the fluctuations around $\theta = 0^\circ$ for different $\tilde{R}$. In Fig. 5 we show the average tilt angle θ as a function of time for Pe = 115 and size ratio $\tilde{R} = 1.3$ (a) and $\tilde{R} = 2.5$ (b). As expected, we observe larger fluctuations as we increase the size ratio $\tilde{R}$: we estimate that $\sigma_\theta = 18^\circ$ for $\tilde{R} = 1.3$, while $\sigma_\theta = 39^\circ$ for $\tilde{R} = 2.5$.

In order to investigate how thermal fluctuations destabilize the alignment of the particle as we vary both the Péclet number and the size ratio, we ran many simulations for $40 \lesssim \mathrm{Pe} \lesssim 500$ and for $1.0 < \tilde{R} \leq 2.5$. By analysing the fluctuations of the angle θ about the equilibrium position $\theta = 0^\circ$, we discriminate three different regimes for the hydrodynamic self-alignment. Our results are summarized in Fig. 6. The black dots display the simulation runs performed at a specific value of Pe and $\tilde{R}$. We compute the σ_θ for each run and linearly interpolate between points to obtain a heatmap. The blue region represents the regime of strong alignment, where $\sigma_\theta \leq 15^\circ$. We delimit this region with a solid black line corresponding to $\sigma_\theta = 15^\circ$. The light blue region represents the regime of weak alignment, where $15^\circ < \sigma_\theta \leq 30^\circ$. Finally, the red region shows the regime of no alignment, where $\sigma_\theta > 30^\circ$, also here delimited by a black line corresponding to $\sigma_\theta = 30^\circ$. For a sufficiently high Péclet number, $\mathrm{Pe} \geq 400$, a change in the size ratio does not affect the angular stability regime of the dumbbell, as the convective flux leads to a strong hydrodynamic torque. We define this range of high Pe as the non-Brownian regime. For $\mathrm{Pe} < 50$ the self-orientation does not occur for any size ratio of the dumbbell. Therefore we define this regime as the Brownian regime. In the intermediate Pe regime, *i.e.* $50 \leq \mathrm{Pe} < 400$, we find all three self-orientation behaviours: upon increasing $\tilde{R}$, the strong alignment region shrinks, whereas the weak and no alignment

 This journal is © The Royal Society of Chemistry 2019

Published on 17 December 2018. Downloaded by Universiteit Utrecht on 1/17/2020 3:31:00 PM.

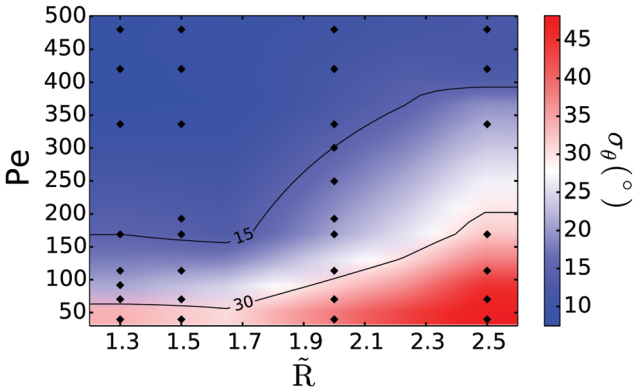

Fig. 6 State diagram of a dumbbell with $s = 8.8\ a_0$ describing the stability of the particle self-alignment along the direction of the fluid flow for different Péclet numbers Pe and size ratios $\tilde{R}$. The characterization of stability is based on the magnitude of the standard deviation $\sigma_\theta = \sqrt{\langle\theta^2\rangle - \langle\theta\rangle^2}$ of θ with respect to its mean value $\langle\theta\rangle$. The blue region denotes oscillations limited to $\sigma_\theta \leq 15°$, where the alignment is strong. The light blue region is characterized by oscillations $15° < \sigma_\theta \leq 30°$ so the alignment is weaker. Finally, the red region denotes oscillations with $\sigma_\theta > 30°$, therefore the alignment is no longer possible in this region. The black dots denote the state points at which the simulations were performed. The heatmap is computed by linear interpolation between these points. The black lines delimit the three regimes of alignment.

regions widen. This confirms our expectations that the stability is also strongly related to the shape of the dumbbell, and provides a quantitative estimation of this dependence. For completeness, we also report the values of σ_θ for the simulated state points in Fig. 7, where we show σ_θ as a function of Pe for different size ratios $\tilde{R}$. We note that small changes in angle cut-offs for defining the stability regions can determine a small shift of the boundaries, but the overall trends remain the same.

On the basis of these results, we extract information on the required experimental conditions to achieve a certain level of alignment. In Table 1, we list the particle radius, ranging from a few microns for macro-colloids, to a few tens of nanometers for nanoparticles. We compute the critical flow rate U_0^c for different

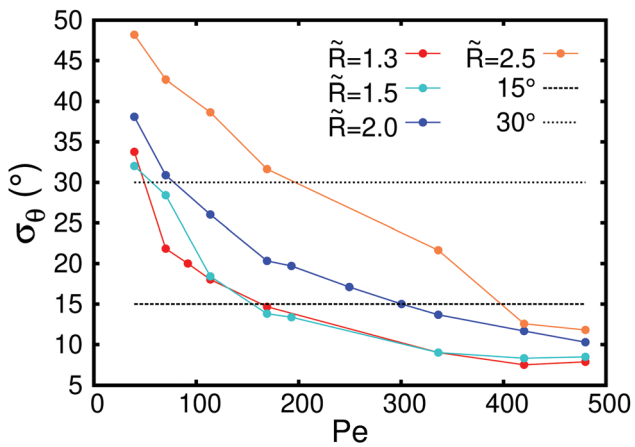

Fig. 7 Standard deviation σ_θ of the tilt angle θ of a dumbbell with $s = 8.8\ a_0$ as a function of Pe for different size ratios $\tilde{R}$. The dashed lines correspond to $\sigma_\theta = 15°$ and $\sigma_\theta = 30°$.

Table 1 Critical flow rate U_0^c (last column) for different particle sizes R_1 (first column) and for different regimes of alignment Pe^c (bottom row). The values $\mathrm{Pe}^c = 50$ and $\mathrm{Pe}^c = 150$ represent the thresholds for weak and strong alignment of a dumbbell with size ratio $\tilde{R} < 1.5$, and $\mathrm{Pe}^c = 400$ represents the threshold for strong alignment of a dumbbell with $\tilde{R} = 2.5$. The corresponding critical flow rates U_0^c are calculated from eqn (10). We also display width W and height H of the channel for each particle size

R_1 (μm)	W (μm)	H (μm)	U_0^c (μm s^{-1})
10	250	25	$(1,3,9) \times 10^{-1}$
5	125	12.5	$(0.4,1,4) \times 10^{0}$
1	25	2.5	$(1,3,9) \times 10^{1}$
0.5	12.5	1.25	$(0.4,1,4) \times 10^{2}$
0.1	2.5	0.25	$(1,3,9) \times 10^{3}$
			$\mathrm{Pe}^c = (50, 150, 400)$

particle sizes R_1 and for different regimes of alignment Pe^c. The values $\mathrm{Pe}^c = 50$ and $\mathrm{Pe}^c = 150$ represent the thresholds for weak and strong alignment of a dumbbell with size ratio $\tilde{R} < 1.5$, and $\mathrm{Pe}^c = 400$ represents the threshold for strong alignment of a dumbbell with $\tilde{R} = 2.5$, as obtained from Fig. 6. We also display width W and height H of the channel for each particle size. For instance, a particle with $R_1 = 0.1$ μm and $\tilde{R} < 1.5$ displays weak alignment for $U_0^c \geq 1 \times 10^3$ μm s^{-1} and $U_0^c < 3 \times 10^3$ μm s^{-1}, while it shows strong alignment for $U_0^c \geq 3 \times 10^3$ μm s^{-1}. In order to observe strong alignment of a particle with the same size and $\tilde{R} = 2.5$, one has to set a flow rate $U_0^c \geq 9 \times 10^3$ μm s^{-1}. The critical flow rates are derived by inverting eqn (8), obtaining

$$U_0^c = \frac{\mathrm{Pe}^c k_B T}{6\pi\eta {R_1}^2}, \tag{10}$$

where D_0 is rewritten in terms of the fluid viscosity through the Stokes–Einstein equation $D_0 = k_B T/(6\pi\eta R_1)$. In our computation, we considered room temperature $T = 300$ K and the viscosity of water $\eta = 0.001$ Pa s. Of course, the pressure drops required to reach these flow velocities increases with decreasing channel dimensions. For a channel of length L_z and a height $H \ll W$, the pressure drop is approximately given by $\Delta p = 12\eta U_0 L_z/H^2$. According to our results, alignment is achieved within a distance of 100 bond lengths s, which is of the order of 100 H. For a channel of this length, the pressure drop is $\Delta p = 1200\eta U_0/H$. For example, for a channel with $H = 0.25$ μm and $L_z = 25$ μm, a pressure drop of 0.5 bar will be sufficient to orient the $R_1 = 0.1$ μm particle. In addition, it has been shown that it is possible to achieve flow rates on the order of mm s^{-1} in nanofluidic devices, as reported in ref. 42 and 43.

3.3 Hydrodynamic self-orientation: the relaxation time

As mentioned earlier, in this section we provide a quantitative analysis of the rate of the self-orientation process. An analytical expression describing how θ evolves with time $\tilde{t}$ was derived for the case of a dumbbell particle composed of two disks instead of two spheres.[22] Even though the two dumbbell models are different, the analytical expression is valid also for the present case of a dumbbell composed of spheres. In fact it has recently been shown that the analytical expression holds for all particles which have the property to be mirror symmetric with respect to

Published on 17 December 2018. Downloaded by Universiteit Utrecht on 1/17/2020 3:31:00 PM.

the xy plane passing through their longitudinal axis.[24] Taking $\tilde{t} = 0$ when $\theta = 90^\circ$, the dependence of θ with respect to $\tilde{t}$ can be expressed implicitly as[22]

$$\tilde{t} = \tilde{\tau} \ln\left(\frac{1 + \cos(\theta)}{\sin(\theta)}\right), \tag{11}$$

where $\tilde{\tau}(\tilde{R}, H, W)$ is the relaxation time defined as the characteristic time the particle spends in self-orienting from $\theta = 90^\circ$ to $\theta = 0^\circ$. This parameter depends on the shape of the particle and the geometry of the channel. This quantity can be extracted by fitting eqn (11) to the data obtained from the numerical simulations. Each simulation run is parametrized by Pe and $\tilde{R}$. We perform eight independent runs to carry out our statistical analysis.

To perform the fit, we first shift each single curve $\theta(\tilde{t})$ in time, such that $\theta = 90^\circ$ corresponds to $\tilde{t} = 0$. It is worth to mention that the time shift is usually different for each curve. This is due to the time delay the particle accumulates before starting the self-orientation. We shift the curves also to perform an accurate averaging of θ over the eight realizations. In fact, this procedure guarantees that we get the best superpositions of the curves for different runs, as the internal hydrodynamic torque is maximal at $\theta = 90^\circ$. We obtain the value of $\tilde{\tau}$ by fitting eqn (11) to each single realization. We then average the values of $\tilde{\tau}$ over eight runs. In Fig. 8(a) we show the decay of the tilt angle θ averaged over the eight realizations as a function of time for different $\tilde{R}$ at Pe = 480, in the non-Brownian regime. Since time is scaled by $\tilde{\tau}$, all curves collapse onto the theoretical master curve. The match with theory is remarkably good. In the inset we represent the values of for different size ratio $\tilde{R}$. The characteristic time of alignment monotonically decreases with increasing size ratio. In fact as the size ratio starts to increase from $\tilde{R} = 1.0$, the hydrodynamic torque also increases leading to a faster convergence to the equilibrium configuration. A similar

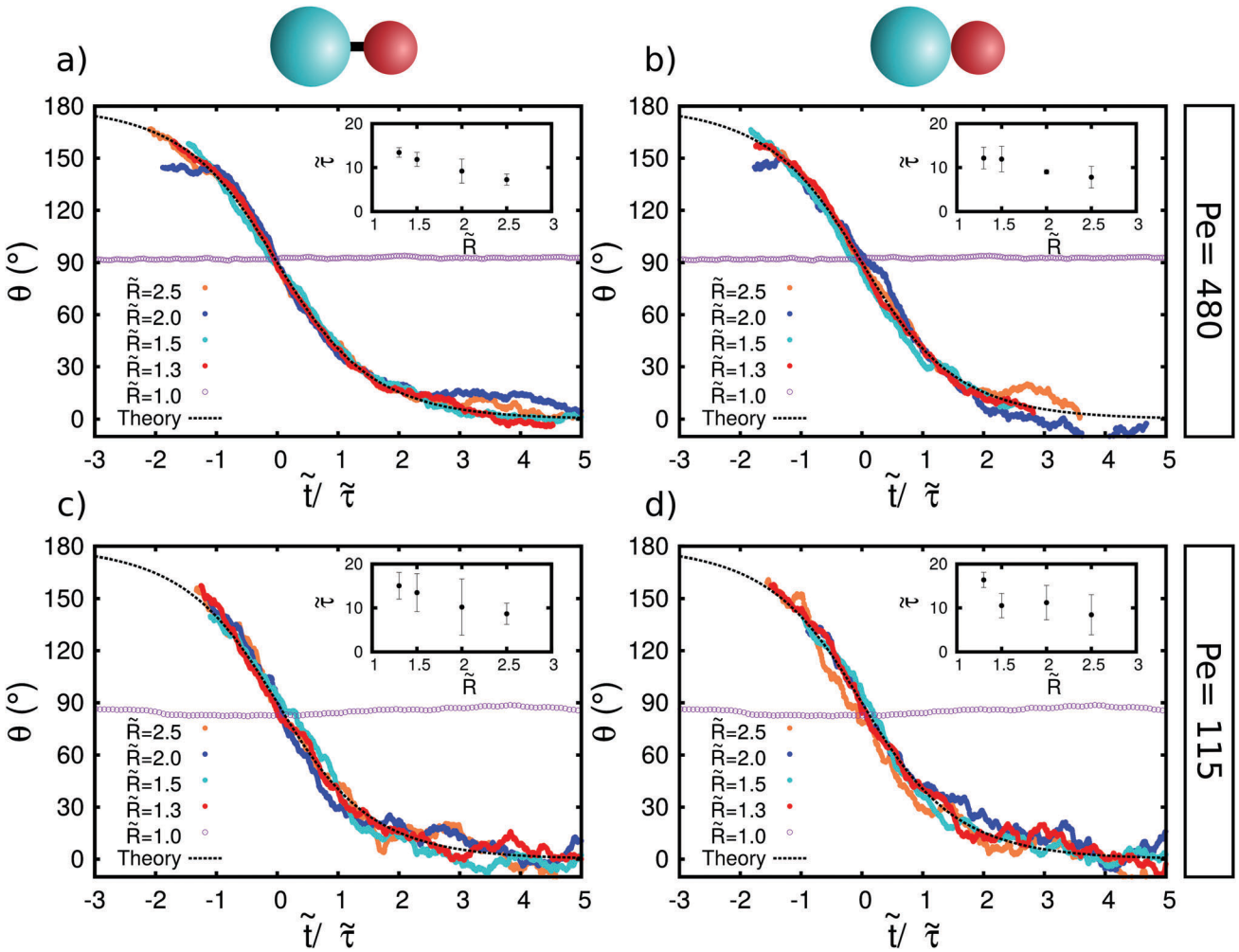

Fig. 8 The average tilt angle θ as a function of rescaled time $\tilde{t}/\tilde{\tau}$. Each coloured curve represents a different size ratio $\tilde{R}$ and is obtained by averaging over eight independent runs. For $\tilde{R} = 1$ the orientation of the dumbbell remains constant in time at $\theta = 90^\circ$, which is the initial orientation. For $\tilde{R} > 1$ we scale the data by a fitted $\tilde{\tau}$, collapsing all the curves onto a master curve predicted by theory and represented here with a black dashed line. The inset shows the fitted relaxation time $\tilde{\tau}$ for different $\tilde{R}$. In the range of $\tilde{R}$ investigated, $\tilde{\tau}$ is a monotonically decreasing function of $\tilde{R}$. (a and b) Results obtained at Pe = 480 by implementing the model with constant $s = 8.8\ a_0$ and the model with $s = R_1 + R_2$, respectively. (c and d) Results obtained at Pe = 115 by implementing the model with constant $s = 8.8\ a_0$ and the model with $s = R_1 + R_2$, respectively. The two models give similar results.

 This journal is © The Royal Society of Chemistry 2019

Published on 17 December 2018. Downloaded by Universiteit Utrecht on 1/17/2020 3:31:00 PM.

trend is shown in Fig. 8(c) where we illustrate the same analysis performed at Pe = 115, in the intermediate regime. We highlight that the only noticeable difference is the presence of small fluctuations within the curves which denotes the relative importance of thermal noise over the hydrodynamic convective drag with respect to the case of the non-Brownian regime. These insets also show that the relaxation time for self-alignment is mostly a function of particle geometry, and not of Péclet number, for intermediate to large Péclet numbers.

We also analyse the robustness of the model with respect to small changes in the design of the dumbbell particle. More specifically, we performed simulations with the model presented in Fig. 1(c) where the dumbbell is composed of spheres with their surfaces at contact as we vary $\tilde{R}$. Hence the fluid is not allowed to flow in between them. The results are shown next to the first model in Fig. 8(b) and (d). We observe that the two models give consistent results and the values of $\tilde{\tau}$ fall in the same range. Therefore we infer that the model of the dumbbell particle is robust within small variation in the design of the particle, and that the small gap between the spheres in the first model does not have any major consequence on the self-orientation phenomenon observed.

In order to assess the effect of the side walls on our results, we also performed simulations in a wider channel, characterized by $W \times H \times L_z = 200 \times 10 \times 400\ a_0^3$ for a few selected state points. We did not observe any statistically significant deviations on the values of $\tilde{\tau}$.

4 Conclusions

In summary, we have performed numerical simulations to analyse the self-orientation process of an asymmetric dumbbell particle in a shallow channel at different hydrodynamic regimes. We have implemented the MD + SRD simulation technique and have verified that this method is able to reproduce the correct velocity profile of the fluid flow.

Next, we have investigated the self-orientation process at different relative strengths of Brownian motion and for different particle shapes by varying Pe and $\tilde{R}$, respectively. We define three regimes of stability by analysing the amplitude of oscillations about the equilibrium position $\theta = 0°$. For Pe $\geq$ 400 the alignment is strong for all $\tilde{R}$. As we lower the Péclet number, 50 $\leq$ Pe $<$ 400, thermal fluctuations start to affect the self-orientation process first at large $\tilde{R}$, and progressively also at lower $\tilde{R}$. The self-alignment process is no longer possible for Pe $<$ 50 for any $\tilde{R}$.

On the basis of these results, we have computed the experimental conditions, such as flow rates and channel dimensions, to achieve alignment of asymmetric particles whose sizes range from tens of microns till a few tens of nanometers. This information can guide future experimental work that focus on nanosized objects in fluid flows.

Moreover, we have computed the time dependence of the orientation angle θ, and compared it with the theoretical prediction derived for the fully non-Brownian regime.[22] Our results are in remarkably good agreement with theory, even for intermediate Pe. We have fitted the analytical curves on our data set, where the fitting parameter is the reorientation relaxation time $\tilde{\tau}$. We find that this parameter is a monotonically decreasing function of $\tilde{R}$. We stress that this result is not in contradiction with recent work where the relaxation time shows a minimum for $\tilde{R}$ = 1.9,[23] since their model of dumbbell particle is fundamentally different from our model. In our model we increase $\tilde{R}$ by decreasing the radius of one sphere, leading to a particle composed of two beads for all $\tilde{R}$. In their model the dumbbell is instead composed of two disks where the center-to-center distance is kept constant and the radius of one disk increases with increasing $\tilde{R}$, thus eventually leading to a particle composed of only one disk for high $\tilde{R}$.

This work has provided evidence that control over particle position and orientation is still possible at intermediate Péclet numbers, where diffusion becomes relevant in addition to convection. Our finding is relevant for scientific applications which rely on controlling dispersions in micron-sized devices at intermediate Pe. In fact, several devices are explicitly designed to operate in this regime[44,45] such as H-filters, which enable separation of species by exploiting the difference in diffusivity of the solute particles.[46] Since the diffusivity plays a key role in this process, it is clear that the range of applicability of these devices is confined to the low-to-intermediate Pe regime. Another fundamental aspect of this study reveals that the self-alignment still occurs at length scales on the order of a few microns to a few tens of nanometers. This finding is quite remarkable as there is no experimental evidence yet, to the best of our knowledge, which proves that hydrodynamic self-interaction can function at such small length scales. Therefore our work paves the way to new methods for particle sorting down to scales of fraction of microns by exploiting diffusivity, hydrodynamic self-interactions and particle shape to govern particle position and orientation.

Conflicts of interest

There are no conflicts to declare.

Acknowledgements

The work was supported by The Netherlands Center for Multiscale Catalytic Energy Conversion (MCEC), a NWO Gravitation program funded by the Ministry of Education, Culture and Science of the government of The Netherlands. G. F. acknowledges W. Uspal, B. Eral, B. Bet, R. van Roij, S. Paliwal and G. Avvisati for fruitful discussions. G. F. thanks C. L. Kennedy for the critical reading of the manuscript.

References

1 D. T. Chiu, A. J. DeMello, D. Di Carlo, P. S. Doyle, C. Hansen, R. M. Maceiczyk and R. C. Wootton, *Chem*, 2017, **2**, 201–223.
2 Z. Liu, Y. Lee, J. H. Jang, Y. Li, X. Han, K. Yokoi, M. Ferrari, L. Zhou and L. Qin, *Sci. Rep.*, 2015, **5**, 1–12.
3 S. Kim, S. Han and J. Lee, *Lab Chip*, 2017, **17**, 2095–2103.

Published on 17 December 2018. Downloaded by Universiteit Utrecht on 1/17/2020 3:31:00 PM.

4 J. Son, R. Samuel, B. K. Gale, D. T. Carrell and J. M. Hotaling, *Biomicrofluidics*, 2017, **11**, 054106.
5 S. Suresh, J. Spatz, J. P. Mills, A. Micoulet, M. Dao, C. T. Lim, M. Beil and T. Seufferlein, *Acta Biomater.*, 2015, **23**, S3–S15.
6 A. Vaziri and A. Gopinath, *Nat. Mater.*, 2008, **7**, 15–23.
7 L. Chen, K. X. Wang and P. S. Doyle, *Soft Matter*, 2017, **13**, 1920–1928.
8 M. Y. Hwang, S. G. Kim, H. S. Lee and S. J. Muller, *Soft Matter*, 2018, **14**, 216–227.
9 M. Caggioni, J. Lenis, A. V. Bayles, E. M. Furst and P. T. Spicer, *Langmuir*, 2015, **31**, 8558–8565.
10 U. D. Schiller, J.-B. Fleury, R. Seemann and G. Gompper, *Soft Matter*, 2015, **11**, 5850–5861.
11 L. Wang, L. A. Flanagan, N. L. Jeon, E. Monuki and A. P. Lee, *Lab Chip*, 2007, **7**, 1114.
12 P. Sajeesh and A. K. Sen, *Microfluid. Nanofluid.*, 2014, **17**, 1–52.
13 C. Y. Wu, K. Owsley and D. Di Carlo, *Adv. Mater.*, 2015, **27**, 7970–7978.
14 D. Stoecklein, C. Y. Wu, D. Kim, D. Di Carlo and B. Ganapathysubramanian, *Phys. Fluids*, 2016, **28**, 012003.
15 D. Stoecklein, K. G. Lore, M. Davies, S. Sarkar and B. Ganapathysubramanian, *Sci. Rep.*, 2017, **7**, 1–11.
16 N. Pamme, *Lab Chip*, 2007, **7**, 1644.
17 X. Xuan, J. Zhu and C. Church, *Microfluid. Nanofluid.*, 2010, **9**, 1–16.
18 D. R. Gossett, W. M. Weaver, A. J. MacH, S. C. Hur, H. T. K. Tse, W. Lee, H. Amini and D. Di Carlo, *Anal. Bioanal. Chem.*, 2010, **397**, 3249–3267.
19 K. K. Zeming, S. Ranjan and Y. Zhang, *Nat. Commun.*, 2013, **4**, 1625–1628.
20 J. Zhang, S. Yan, R. Sluyter, W. Li, G. Alici and N. T. Nguyen, *Sci. Rep.*, 2014, **4**, 1–9.
21 M. Masaeli, E. Sollier, H. Amini, W. Mao, K. Camacho, N. Doshi, S. Mitragotri, A. Alexeev and D. Di Carlo, *Phys. Rev. X*, 2012, **2**, 1–13.
22 W. E. Uspal, H. Burak Eral and P. S. Doyle, *Nat. Commun.*, 2013, **4**, 2666.
23 B. Bet, R. Georgiev, W. Uspal, H. B. Eral, R. V. Roij and S. Samin, *Microfluid. Nanofluid.*, 2018, **22**, 1–12.
24 B. Bet, S. Samin, R. Georgiev, H. B. Eral and R. van Roij, *J. Phys.: Condens. Matter*, 2018, **30**, 224002.
25 D. Stein, F. H. J. van der Heyden, W. J. A. Koopmans and C. Dekker, *Proc. Natl. Acad. Sci. U. S. A.*, 2006, **103**, 15853–15858.
26 J. Hansen and I. McDonald, *Theory of simple liquids*, Academic Press, London, 2nd edn, 1986.
27 M. P. Allen and D. J. Tildesley, *Computer simulation of liquids*, Claredon Press, Oxford, Oxford, 1987.
28 A. Malevanets and R. Kapral, *J. Chem. Phys.*, 1999, **110**, 8605.
29 A. Malevanets and R. Kapral, *J. Chem. Phys.*, 2000, **112**, 7260.
30 A. Lamura, G. Gompper, T. Ihle and D. M. Kroll, *Europhys. Lett.*, 2001, **56**, 768.
31 M. A. Webster and J. M. Yeomans, *J. Chem. Phys.*, 2005, **122**, 164903.
32 J. T. Padding and A. A. Louis, *Phys. Rev. Lett.*, 2004, **93**, 220601.
33 J. T. Padding and A. A. Louis, *Phys. Rev. E: Stat., Nonlinear, Soft Matter Phys.*, 2006, **74**, 1–29.
34 T. Ihle and D. M. Kroll, *Phys. Rev. E: Stat., Nonlinear, Soft Matter Phys.*, 2001, **63**, 0202011.
35 T. Ihle and D. M. Kroll, *Phys. Rev. E: Stat., Nonlinear, Soft Matter Phys.*, 2003, **67**, 066705.
36 D. Heyes, *Chem. Phys.*, 1983, **82**, 285–301.
37 M. Hecht, J. Harting, T. Ihle and H. J. Herrmann, *Phys. Rev. E: Stat., Nonlinear, Soft Matter Phys.*, 2005, **72**, 1–16.
38 E. Guyon, J. P. Hulin, L. Petit and C. D. Mitescu, *Physical Hydrodynamics*, Oxford University Press, Oxford, 2001.
39 M. Sano and K. Tamai, *Nat. Phys.*, 2016, **12**, 249–253.
40 J. P. Matas, J. F. Morris and É. Guazzelli, *Phys. Rev. Lett.*, 2003, **90**, 4.
41 M. Spiga and G. L. Morino, *Int. Commun. Heat Mass Transfer*, 1994, **21**, 469–475.
42 E. Tamaki, A. Hibara, H. Kim, M. Tokeshi and T. Kitamori, *J. Chromatogr. A*, 2006, **1137**, 256–262.
43 F. Liang, Y. Qiao, M. Duan, N. Lu, J. Tu and Z. Lu, IEEE International Conference on Manipulation, Manufacturing and Measurement on the Nanoscale (3M-NANO), 2018, pp. 32–36.
44 A. Hatch, A. E. Kamholz, K. R. Hawkins, M. S. Munson, E. A. Schilling, B. H. Weigl and P. Yager, *Nat. Biotechnol.*, 2001, **19**, 461–465.
45 T. M. Squires and S. R. Quake, *Rev. Mod. Phys.*, 2005, **77**, 977–1026.
46 J. P. Brody and P. Yager, *Sens. Actuators, A*, 1997, **58**, 13–18.

 This journal is © The Royal Society of Chemistry 2019